First-principles study of transport in WO₃

Wennie Wang 0, 1,* Youngho Kang, 1,† Hartwin Peelaers 0, 1,‡ Karthik Krishnaswamy 0, 2,8 and Chris G. Van de Walle 01 ¹Materials Department, University of California, Santa Barbara, California 93106-5050, USA 2 Electrical and Computer Engineering Department, University of California, Santa Barbara, California 93106-5050, USA

(Received 20 September 2019; revised manuscript received 23 December 2019; published 13 January 2020)

We investigate the transport properties of tungsten trioxide (WO₃) from first principles. The full \mathbf{k} dependence of the scattering rate is included, and electron mobilities as a function of doping are calculated using Boltzmann transport theory. Our predicted room-temperature mobility is as high as 485 cm² V⁻¹ s⁻¹ at 10²⁰ cm⁻³ doping, which makes WO₃ a promising material for device applications. We elucidate why the mobility is so much higher in WO₃ compared to the prototype perovskite oxide SrTiO₃ based on an analysis of the electronic and vibronic structure.

DOI: 10.1103/PhysRevB.101.045116

I. INTRODUCTION

Perovskite oxides with the chemical formula ABO_3 , where A and B are metal cations, have garnered substantial interest for potential applications in novel electronic devices; they also exhibit a rich variety of physical phenomena [1,2]. Tungsten trioxide (WO₃) belongs to this class of materials, but with a vacant A site. WO₃ is well-known for its electrochromism [3–5], in which the transmittance at infrared and visible wavelengths can be controlled by intercalation of donor ions such as Li [6] or Na [7]. WO₃ also acts as a functional material in gas sensing [8], photocatalysis [9,10], and as an electrode in lithium-ion batteries [11]. It has also been utilized in high-efficiency solar cells, where WO₃ serves as the electron transport layer [12].

In all these applications, carrier transport plays a pivotal role, and a full understanding of transport mechanisms is a prerequisite for device performance. Few studies have been devoted to understanding transport in WO₃; mainly these have been experimental reports of mobilities or electrical resistivities with fits to models. For instance, Berak et al. [13] reported mobilities in single-crystalline monoclinic WO₃ on the order of tens of cm² V⁻¹ s⁻¹ near room temperature, and Berggren studied the influence of temperature on resistivities of lithiated samples [14]. Here, we use a fully firstprinciples approach to shed light on the microscopic origins of

WO₃ has various polymorphs [15], which are distinguished by the degree of tilting, rotation, and distortion of WO₆ octahedra. In this work, we focus on the cubic phase [Fig. 1(a)], which is free of structural distortions. We are motivated to study the cubic phase because of its potential use in complex oxide heterostructures in combination with other cubic perovskites; complex oxide interfaces can lead to large twodimensional electron gas densities [16,17]. Controlled growth along the [100] direction of cubic WO₃ on SrTiO₃ (STO) has been demonstrated using molecular beam epitaxy [18] and dc magnetron sputtering [19]. The cubic phase may also be stabilized through doping with donor species such as Li, Na, or K [6,20], a phenomenon that has been shown to be driven by the presence of excess electrons [21,22]. Exploring transport in cubic WO3 is therefore relevant for bulk as well as epitaxial films.

We use first-principles calculations based on density functional theory (DFT) to obtain electronic and vibrational spectra, and calculate mobilities using Boltzmann transport theory within the relaxation time approximation [23]. We consider electron-phonon interactions as the dominant scattering mechanism at room temperature [23]. As WO₃ is a polar material, we discuss the role of LO-phonon scattering. Due to the heavy mass of the tungsten atom, spin-orbit coupling (SOC) is included in our calculations. We use Wannier interpolation [24,25] to account for the k-dependent scattering rate on large grids [26,27].

Our results show that the room-temperature mobility is much higher than in other complex oxides: at 10^{20} cm⁻³ doping, the mobility is as high as $485 \text{ cm}^2 \text{ V}^{-1} \text{ s}^{-1}$ when screening due to the conduction electrons is included. This is more than an order of magnitude larger than in the prototype perovskite complex oxide, SrTiO₃ (STO) [16,28,29]. A detailed comparison of the various features in the electronic and vibronic structure will allow us to elucidate the factors that contribute to this difference in mobilities.

After a presentation of our methodology in Sec. II A, we first present our results on the bulk electronic and vibronic properties of cubic WO₃ in Secs. III A and III B. In Sec. IIIC, we present an in-depth investigation of scattering rates and (unscreened) mobilities as a function of doping. Finally, in Sec. IIID, we address why the roomtemperature mobility in WO₃ is significantly higher than in cubic STO.

^{*}wwwennie@engineering.ucsb.edu; Present address: University of Chicago, Chicago, Illinois 60637 USA.

[†]Present address: Korea Institute of Materials Science, Changwonsi South Korea.

[‡]Present address: University of Kansas, Lawrence, KS 66045, USA.

[§]Present address: Advanced Design, Intel Corporation, Hillsboro, OR 97124, USA.

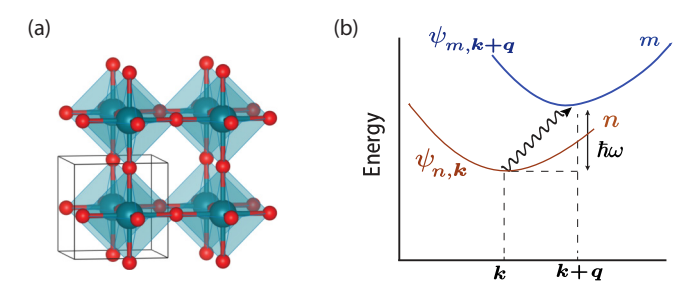


FIG. 1. (a) Crystal structure of cubic WO₃. Tungsten atoms are shown in blue and oxygen atoms in red. (b) Schematic representation of electron-phonon scattering, in which a carrier initially in state $\psi_{n,\mathbf{k}}$ scatters to state $\psi_{m,\mathbf{k}+\mathbf{q}}$ with the assistance of a phonon with frequency ω and wave vector \mathbf{q} .

II. METHODOLOGY

A. Calculation methods

Our calculations are based on density functional theory using the QUANTUM ESPRESSO code [30] with norm-conserving pseudopotentials [31] and the exchange-correlation functional of Perdew, Burke, and Ernzerhof (PBE) [32]. For W, the 5p6s5d states are treated as valence states, and for O, the 2s2p states. In our STO calculations, the 4s4p5s states are treated as valence states for Sr and 3s3p3d4s for Ti. In order to assess the accuracy of our band structures, we also use the hybrid functional of Heyd, Scuseria, and Ernzerhof (HSE) [33,34]. To include SOC, we perform self-consistent calculations based on a fully relativistic pseudopotential. We use a plane-wave cutoff of 125 Ry and a $6 \times 6 \times 6$ k-point grid for integrations over the Brillouin zone.

The vibrational spectra are calculated using density functional perturbation theory (DFPT) [35]. Using a hybrid functional for all aspects of the calculations is currently not feasible, since DFPT calculations are not implemented with hybrid functionals; we therefore use the PBE functional. Based on the lattice dynamical properties we obtain the electron-phonon matrix elements, which describe the strength of phononmediated transitions between different electronic states. These are calculated on a $6 \times 6 \times 6$ k- and q-point grids, and then Wannier-interpolated at denser k- and q-point grids using the EPW code [26]. For calculating the scattering rates and mobility, we use $50 \times 50 \times 50$ k- and q-point grids. Mobilities changed by less than 10% for grids up to $80 \times 80 \times 80$. We neglect the imaginary modes in the mobility calculations by setting the matrix elements for such modes to 0. However, as shown for SrTiO₃ in a previous work [36], their impacts on the room temperature mobility are expected to be negligible compared to those of polar LO modes. Finally, we note that finite temperature may lead to band-gap renormalization in WO₃ not present in our calculations, but expect qualitative conclusions for higher mobilities in WO₃ compared to STO to hold.

B. Electrical conductivity and mobility

In a cubic crystal, the mobility is isotropic. We compute the conductivity tensor based on Boltzmann transport theory [23] using the implementation described in Ref. [29]:

$$\sigma_{\alpha\beta} = \frac{e^2}{V_{\text{cell}}} \sum_{n,\mathbf{k}} w_{\mathbf{k}} \tau_{n\mathbf{k}} \left(-\frac{\partial f_{n,\mathbf{k}}}{\partial \epsilon_{n,\mathbf{k}}} \right) v_{n\mathbf{k},\alpha} v_{n\mathbf{k},\beta} , \qquad (1)$$

where $w_{\mathbf{k}}$ is the **k**-point weight, V_{cell} is the cell volume, $f_{n,\mathbf{k}}$ is the Fermi-Dirac distribution function, and $v_{n\mathbf{k}} \equiv 1/\hbar \times \partial \epsilon_{n,\mathbf{k}}/\partial \mathbf{k}$ are band velocities. When spin-orbit coupling is included, the sum over n implicitly includes a sum over total angular momentum $(j = l \pm 1/2)$ states [37]. The conductivity is divided by the carrier concentration n to obtain mobility, $\mu = \frac{\sigma}{n^2}$.

C. Scattering rate

When calculating electronic conductivity, it is common to assume a constant scattering rate τ^{-1} [38]. First-principles approaches in which the energy and **k** dependence of the scattering rate are fully taken into account have recently emerged [29,36,39–43]. These studies have shown that the scattering rate has a strong dependence on band and **k** vector that must be taken into account. In our calculations, the band- and **k**-dependent scattering rate $\tau_{n,\mathbf{k}}^{-1}$ is calculated using [29]

$$\tau_{n\mathbf{k}}^{-1} = \frac{2\pi}{\hbar} \sum_{\mathbf{q}\nu,m} |g_{mn,\nu}(\mathbf{k}, \mathbf{q})|^2$$

$$\times \{ (n_{\mathbf{q}\nu} + f_{\mathbf{k}+\mathbf{q},m}) \, \delta(\epsilon_{\mathbf{k}+\mathbf{q},m} - \epsilon_{\mathbf{k},n} - \hbar\omega_{\mathbf{q}\nu}) + (1 + n_{\mathbf{q}\nu} - f_{\mathbf{k}+\mathbf{q},m}) \, \delta(\epsilon_{\mathbf{k}+\mathbf{q},m} - \epsilon_{\mathbf{k},n} + \hbar\omega_{\mathbf{q}\nu}) \}, \quad (2)$$

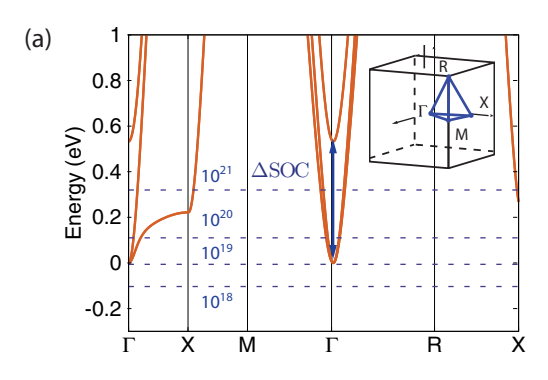
where $g_{mn,\nu}(\mathbf{k}, \mathbf{q})$ are electron-phonon coupling matrix elements, and $n_{\mathbf{q}\nu}$ and $f_{m,\mathbf{k}+\mathbf{q}}$ are phonon and electron occupation factors, which are described by Bose-Einstein and Fermi-Dirac distributions. Bands are indexed by m and n, while phonons are indexed by wave vector \mathbf{q} and frequency ν . The δ functions ensure energy conservation in the electron-phonon scattering processes.

D. Electron-phonon matrix elements

The scattering rate in Eq. (2) includes contributions from all phonons. However, scattering off polar longitudinal optical (LO) phonons is a dominant scattering mechanism at room temperature in polar materials [23,29,42,43], and also requires special attention in the numerical treatment. Electrons couple to the long-range macroscopic electric fields that arise from the out-of-phase motion of the atoms associated with LO modes, and this is described by the electron-phonon matrix elements. LO-phonon scattering gives rise to diverging electron-phonon matrix elements as $\mathbf{q} \to 0$ [29,44]; the long-range contribution is treated separately in the computational approach [26,27].

The electron-phonon matrix elements $g_{mn,\nu}(\mathbf{k}, \mathbf{q})$ are calculated for transitions from the initial electronic state $\psi_{n,\mathbf{k}}$ to the final state $\psi_{m,\mathbf{k}+\mathbf{q}}$ [see Fig. 1(b)] using [26,45,46]

$$g_{mn,\nu}(\mathbf{k},\mathbf{q}) = g_{mn,\nu}^{S}(\mathbf{k},\mathbf{q}) + g_{mn,\nu}^{L}(\mathbf{k},\mathbf{q}), \qquad (3)$$



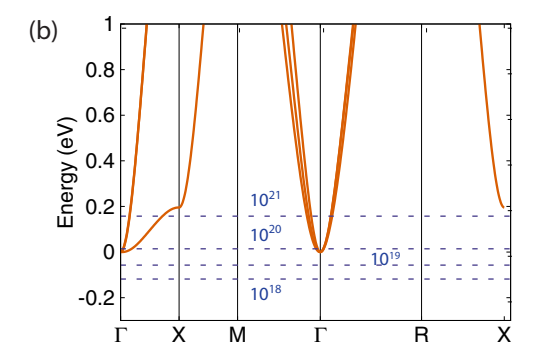


FIG. 2. Electronic band structure of (a) cubic WO₃ and (b) cubic strontium titanate (STO). The Brillouin zone, identifying high-symmetry points, is depicted in the inset. Only the t_{2g} conduction-band states are shown. Dashed lines indicate the Fermi level for various electron concentrations (in cm⁻³). The band splitting due to spin-orbit coupling in WO₃ is Δ SOC = 0.55 eV.

where $g_{mn,\nu}^S$ is the short-range contribution, and the long-range contribution $g_{mn,\nu}^L$ is calculated as [26]

$$g_{mn,\nu}^{L}(\mathbf{k},\mathbf{q}) = i \frac{e^{2}}{\Omega \varepsilon_{0}} \sum_{j} \sqrt{\frac{\hbar}{2M_{j}\omega_{\mathbf{q},\nu}}}$$

$$\times \sum_{\mathbf{G} \neq \mathbf{q}} \frac{(\mathbf{q} + \mathbf{G}) \cdot \mathbf{Z}_{j}^{*} \cdot \mathbf{e}_{j,\nu}(\mathbf{q})}{(\mathbf{q} + \mathbf{G}) \cdot \boldsymbol{\epsilon}^{\infty} \cdot (\mathbf{q} + \mathbf{G})}$$

$$\times \langle \psi_{m,\mathbf{k}+\mathbf{q}} | e^{i(\mathbf{q}+\mathbf{G}) \cdot \mathbf{r}} | \psi_{n,\mathbf{k}} \rangle, \qquad (4)$$

with Ω the volume of the cell, **G** a reciprocal lattice vector, Z_i^* the Born effective charge tensor for atom j with mass M_i , $\mathbf{e}_{i,\nu}(\mathbf{q})$ the polarization vector associated with phonon wave vector \mathbf{q} of mode ν , and ϵ^{∞} the macroscopic high-frequency dielectric tensor. For the cubic phase, there is only one unique element. The electron-phonon matrix elements are weighted by the overlap factor between initial and final electronic states, $\langle \psi_{m,\mathbf{k}+\mathbf{q}}|e^{i(\mathbf{q}+\mathbf{G})\cdot\mathbf{r}}|\psi_{n,\mathbf{k}}\rangle$. Inclusion of the overlap factor results in up to 33% enhancement in mobility. Previous calculations on GaAs [46], SnO₂ [47], GaN [48], and various oxides [29,39,42,43] have shown such analytic models, including those proposed by Fröhlich [44] and Vogl [45], can successfully describe $g_{mn,\nu}^L$ for polar materials. To check the validity of using interpolation with Wannier functions [including using Eq. (4) for the long-range component, we compared the phonon spectra and electron-phonon matrix elements with explicit DFPT calculations along the high-symmetry paths of the Brillouin zone and found excellent agreement.

We additionally consider free-carrier screening due to the presence of electrons in the conduction band. The screening wave vector is calculated using Thomas-Fermi theory, as described in Ref. [42], and is included in the calculation of the electron-phonon matrix elements as described in Ref. [49].

III. RESULTS

A. Bulk electronic and vibronic properties

We first present the electronic and vibronic structure of WO₃. The calculated lattice parameter is a = 3.80 Å, within 0.5% of reported experimental values (a = 3.77 Å [50] and a = 3.78 Å [7]). The calculated band structure for the conduction band is shown in Fig. 2(a). The comparison with the band structure of STO [Fig. 2(b)] will be discussed in Sec. III D.

The conduction bands are composed predominantly of W 5d states. In cubic perovskites, the crystal field due to the octahedral oxygen cage encasing the transition-metal atom causes the d states to split into the lower-lying triply-degenerate t_{2g} and higher-lying doubly-degenerate e_g states. The inclusion of SOC splits the t_{2g} degeneracy and lifts one of the bands by 0.55 eV relative to the conduction-band minimum (CBM). The fundamental gap is $E_g = 0.70$ eV for nonrelativistic calculations of WO₃ (consistent with previous PBE values [51]) and $E_g = 0.51$ eV with SOC included.

While PBE is known to underestimate the band gap, only the conduction-band structure near the Fermi level is relevant for determining transport properties of electrons. We do want to establish that the band dispersions obtained in PBE are reliable. For that purpose we compare with a band structure obtained with the HSE hybrid functional, which has been shown to provide a reliable description of the electronic structure of solids [52], and has been previously used to obtain band structures for WO₃ [53]. In Table I, we compare effective masses calculated based on the PBE band structure with values obtained using HSE. Effective masses were calculated by fitting the band structure to a hyperbolic model as derived from $\mathbf{k} \cdot \mathbf{p}$ theory [54]:

$$\hbar^2 k^2 / 2m_{\Gamma}^* = \epsilon_{\mathbf{k}} (1 + \alpha \epsilon_{\mathbf{k}}), \tag{5}$$

where m_{Γ}^* is the electron effective mass at Γ , $\epsilon_{\mathbf{k}}$ is the band energy and momentum, and α is the nonparabolicity parameter. The comparison indicates that PBE provides a reliable band structure. The SOC-induced splitting results in

TABLE I. Effective masses of the t_{2g} states for cubic WO₃ along high-symmetry directions, in units of the free electron mass m_0 . Effective masses m_i^* are indexed by band i, starting from the lowestlying band. Values calculated with PBE and HSE [53] functionals are shown.

	$\Gamma \to X$		$\Gamma o M$		$\Gamma \to R$	
	PBE	HSE	PBE	HSE	PBE	HSE
$\overline{m_1^*}$	0.17	0.17	0.24	0.22	0.21	0.18
m_2^*	0.15	0.18	0.15	0.17	0.15	0.14
$m_2^* \\ m_3^*$	0.21	0.20	0.25	0.26	0.20	0.17

TABLE II. Calculated longitudinal (LO) and transverse (TO) phonon frequencies in cm $^{-1}$ (meV in parentheses) for WO $_3$ and STO at Γ .

a	LO	$\omega_{ extsf{T}}$	o
WO_3	STO	WO_3	STO
892 (111)	796 (99)	570 (70)	560 (69)
387 (48)	448 (55)	292i (36i)	169 (21)
	161 (20)		25 (3)

the originally heavy band along $\Gamma \to X$ to have an effective mass comparable to the other t_{2g} bands.

The cubic phase contains four atoms in the unit cell, leading to 12 phonon modes, including two longitudinal optical (LO) phonons and four transverse optical (TO) phonon modes. Our calculated frequencies for polar optical modes at Γ are shown in Table II. The polar optical modes are associated with one LO and two degenerate TO modes. The imaginary TO mode indicates that the cubic structure is in fact dynamically unstable. Our calculated frequencies at Γ compare reasonably with previous calculations [55].

The calculated phonon frequencies at Γ for STO are also listed in Table II. In contrast to WO₃, STO has 15 phonon modes, including three LO modes and six TO modes. Our calculated frequencies compare well with previous computational studies [29] and with experiment [56,57], despite cubic STO also being dynamically unstable in first-principles calculations.

The calculation of electron-phonon matrix elements [Eq. (4)] requires the high-frequency dielectric constant. Our calculations yield $\varepsilon^{\infty}=10.14$. As a check, we performed calculations for the room-temperature monoclinic phase; averaging over the principal Cartesian directions we find $\varepsilon^{\infty}=5.75$. This compares well with the experimentally measured value of $\varepsilon^{\infty}=5$ [58]. In STO, we calculate $\varepsilon^{\infty}=6.41$ (experiment: $\varepsilon^{\infty}=5.59$, Ref. [59]).

B. Electron-phonon matrix elements

We next present our results for electron-phonon matrix elements. While all phonon modes are included in our calculations, we focus on the polar LO modes as they significantly impact mobility at room temperature [23].

In Fig. 3, we plot the electron-phonon matrix elements for the LO modes along the high-symmetry paths of the Brillouin zone. As expected from Eq. (4), we observe a 1/q dependence in the matrix elements for small q. Deviations from the 1/q behavior away from Γ in Fig. 3 arise from the short-range contribution $g_{mn,\nu}^S$. The plot includes all scattering processes. For interband transitions, the magnitude of the matrix element in Eq. (4) is suppressed; transitions between states with different band indices are weaker due to the overlap factor $\langle \psi_{m,\mathbf{k}+\mathbf{q}}|e^{i(\mathbf{q}+\mathbf{G})\cdot\mathbf{r}}|\psi_{n,\mathbf{k}}\rangle$, which is typically less than unity.

C. Scattering rate and mobility

Using the calculated electron-phonon matrix elements [Eq. (3)], we evaluate the scattering rates of the conduction electrons [Eq. (2)]. In Fig. 4, we plot the scattering rates as a

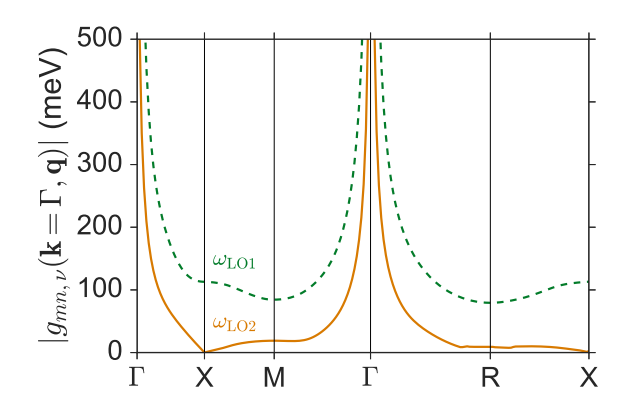


FIG. 3. Magnitude of electron-phonon matrix elements $|g_{mn,\nu}(\mathbf{k},\mathbf{q})|$ plotted along high-symmetry \mathbf{q} points for $\mathbf{k}=\Gamma$ in WO₃. Values are shown for the highest (dashed green) and second-highest LO polar (solid orange) modes and for transitions amongst t_{2g} states. $|g_{mn,\nu}|$ is averaged over all degenerate electronic and vibronic states.

function of electron energy referenced to the CBM with and without screening; we also show the position of the Fermi level. The scattering scales approximately with the electronic density of states, as previously reported for Si [26] and GaAs [60].

Only states with energies close to the Fermi level are involved in scattering. As evident from Eq. (1), this is due to the factor $(-\frac{\partial f_{nk}}{\partial \epsilon_{nk}})$, which is nonzero only in a range of a few k_BT (around 0.2 eV for room-temperature) around the Fermi level and falls rapidly away from the Fermi level.

For 10¹⁸ and 10¹⁹ cm⁻³ doping, we see in Fig. 4 that the main difference in relevant scattering events within the energy window of interest is due to the position of the Fermi level. As the Fermi level becomes degenerate with the conduction band, there are now electronic states above and below the Fermi level that can contribute to scattering. Thus, for 10²⁰ and 10²¹ cm⁻³ doping, scattering events exist both above

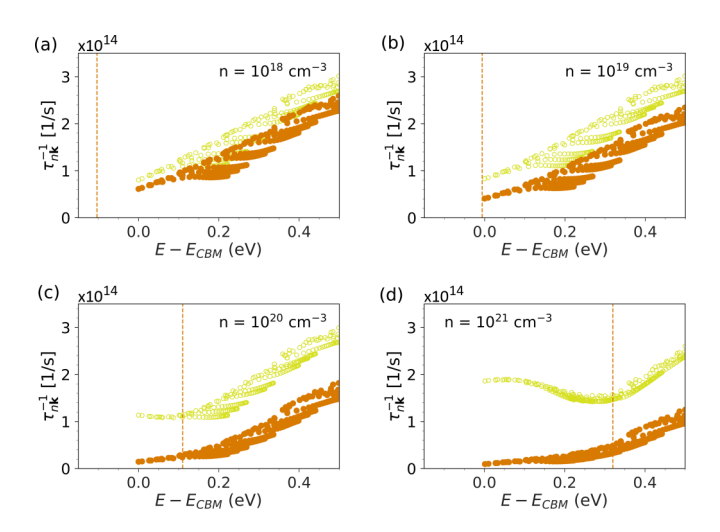


FIG. 4. The electron-phonon scattering rate in cubic WO₃ for (a) 10^{18} , (b) 10^{19} , (c) 10^{20} , and (d) 10^{21} cm⁻³ doping. Hollow golden markers correspond to unscreened τ^{-1} ; solid orange markers correspond to screened τ^{-1} . Electron energies are referenced to the CBM. The Fermi level is indicated with a dotted line.

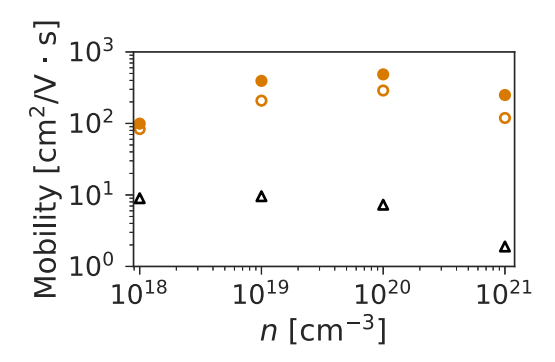


FIG. 5. Calculated mobilities in cm 2 V $^{-1}$ s $^{-1}$ for WO $_3$ as a function of electron doping. Screened mobilities are shown with orange filled circles, unscreened mobilities with orange hollow circles. For comparison, the (unscreened) mobilities of STO are shown with black hollow triangles.

and below the Fermi level. The scattering rate increases for $10^{21}~\rm cm^{-3}$ compared to $10^{20}~\rm cm^{-3}$, since more states become available for scattering. This leads to a decrease in the mobility.

The unscreened and screened mobilities are plotted in Fig. 5 and tabulated in Table III. The unscreened mobilities for WO₃ range between 83 and 289 cm² V⁻¹ s⁻¹ for doping levels between 10¹⁸ and 10²¹ cm⁻³. The trends in mobility as a function of carrier concentration can be understood by considering both the scattering rates (Fig. 4) and the band velocities (Fig. 6) [see Eq. (1)]. When the carrier concentration is increased from 10¹⁸ to 10¹⁹ cm⁻³, conduction-band states at higher energy become occupied, which leads to higher band velocities (Fig. 6). These higher velocities more than compensate for the increase in scattering, thus leading to higher mobility. When the carrier concentration is increased further to 10^{20} cm⁻³, the increase in scattering rate counteracts the increase in band velocities, so that the mobility increases only by a small amount. Increasing the carrier concentration to 10^{21} cm⁻³ leads to a decrease in the mobility, as the increase in band velocities is overshadowed by the increase in scattering.

Including effects due to screening by conduction electrons enhances the mobilities. The screening wave vectors are included in Table III. The enhancement in mobility increases with the screening wave vector when the Fermi level lies below the conduction band. For degenerate doping, screening still enhances mobility, but the increase in scattering events ultimately leads to a decrease in mobility at the highest doping level.

TABLE III. Calculated mobilities in cm² V⁻¹ s⁻¹ for WO₃ and STO as a function of electron doping. For calculations that include screening the screening wave vector q_{scr} is listed in units of 1/Å.

$n (\mathrm{cm}^{-3})$	WO ₃	WO ₃ screened	$q_{ m scr}$	STO
1018	83.3	99.3	0.005	9.0
10^{19}	208	393	0.031	9.6
10^{20}	289	485	0.110	7.3
10^{21}	119	249	0.329	1.9

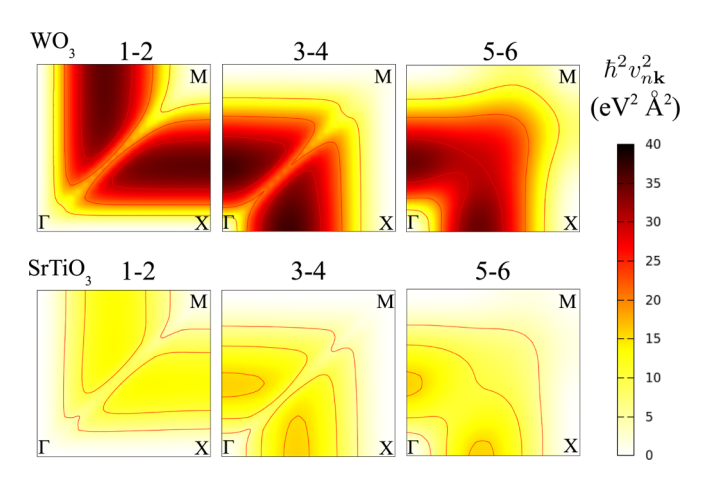
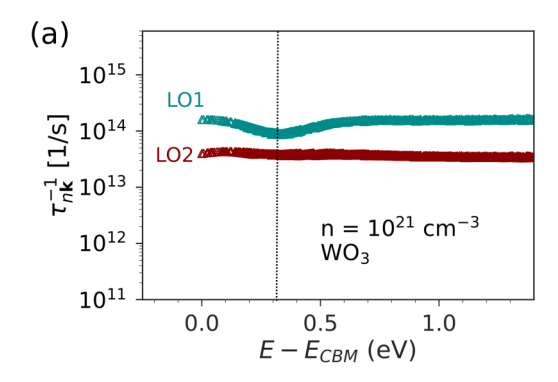


FIG. 6. Band velocity v_{nk}^2 values plotted in the $k_z = 0$ plane in the Brillouin zone, comparing WO₃ and STO. High-symmetry points in the Brillouin zone are indicated. Each of the t_{2g} states is shown, with the number above each panel indicating the corresponding band index, counting from the lowest conduction band. Band indices correspond to spin channels.

D. Comparison with SrTiO₃

We now compare the results for WO₃ with STO. STO is the prototypical perovskite oxide with conduction bands derived from d states. In our calculations for STO we consider the cubic phase and neglect the effects of SOC, since it is very small (\triangle SOC = 0.028 eV, Refs. [61,62]). Indeed, our tests indicate that explicit inclusion of SOC in STO does not significantly the results. Our aim here is not to obtain the highest quantitative accuracy, but to provide physical insights. For fair comparison, the transport properties of STO were obtained using the same methodology as for WO₃. The mobility of STO in the present work is smaller than earlier calculations because of some differences in calculation details. For instance, Ref. [36] additionally incorporated thermal renormalization of the phonon frequencies and iterative solution of the Boltzmann transport equation. In Ref. [29], only the long-range part of the electron-phonon matrix elements was taken into account. These previous studies also used different k- and q-point meshes. Our calculated mobilities for STO are around $10 \text{ cm}^2 \text{ V}^{-1} \text{ s}^{-1}$ for doping levels up to $n = 10^{20} \text{ cm}^{-3}$, much lower than the values for WO₃ (see Table III). This difference can be attributed to a difference in scattering rates, as well as to a difference in effective masses, which are related to the band velocities in Eq. (1).

Our calculated scattering rate $\tau_{n\mathbf{k}}^{-1}$ in STO is $\sim 10^{15}$ s⁻¹ for nondegenerate doping and can increase up to 10^{16} s⁻¹ at $n=10^{21}$ cm⁻³, significantly larger than that in WO₃ (see Fig. 4). We have inspected the electron-phonon coupling strengths [Eq. (3)] for the LO modes and found they are comparable in magnitude between WO₃ and STO. The electron-phonon matrix elements are proportional to the Born effective charge and inversely proportional to the high-frequency dielectric constant. WO₃ has larger Born effective charges compared to STO, and this compensates for the difference in dielectric constants, resulting in comparable electron-phonon coupling strengths. Thus this enhanced scattering rate is due to other factors; we have identified two contributions.



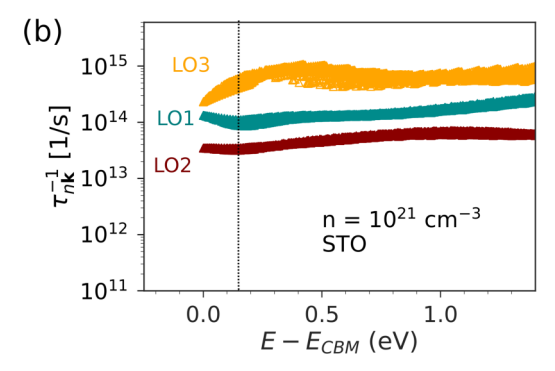


FIG. 7. Mode-resolved scattering rates for the longitudinal optical (LO) phonon modes in (a) WO₃ and (b) STO. LO modes are indexed from highest to lowest frequency. The Fermi level is indicated with a dotted line.

First, the number and frequencies of LO modes. In WO₃ the number of polar LO modes is two, compared to three in STO; this is a result of the missing A-site atom in WO₃. Therefore one fewer scattering channel enters in Eq. (2). The frequencies of the three LO modes in STO are listed in Table II. The additional LO mode in STO actually has the lowest frequency, $\omega_{\text{LO},3} = 161 \text{ cm}^{-1}$ (20 meV), which means that the room-temperature phonon occupation factor will be significantly higher, and this mode will contribute strongly to scattering. This is confirmed by the mode-resolved scattering rates shown in Fig. 7. The scattering rates for the highest two LO modes in WO₃ and STO are comparable, and the additional LO mode in STO corresponds to the highest scattering rate.

Second, the conduction-band states in STO are comprised of Ti 3d states, as opposed to W 5d states in WO₃. W 5d orbitals are less localized than 3d orbitals of Ti, leading to larger bandwidths, more dispersion, and larger band velocities in WO₃. As Eq. (1) depends quadratically on band velocities, this has a substantial effect on the electrical conductivity. The

effect of 3d versus 5d band character can be observed in the effective masses. The effective masses (in units of the free electron mass, and calculated with inclusion of spin-orbit coupling, Ref. [61]) for the three lowest-lying conduction bands along the $\Gamma \to X$ direction in STO are 0.99, 0.39, and 0.55; along the $\Gamma \to M$ direction the values are are 0.74, 0.46, and 0.56. As can be seen from Table I, these effective masses are a factor of two or more larger than those in WO₃.

These effective masses probe the band structure only in the vicinity of the CBM; band dispersion at higher energies also plays a role in mobilities, particularly at higher doping levels. We therefore explicitly inspect band velocities $v_{n\mathbf{k}}^2$ throughout the Brillouin zone, as plotted in Fig. 6. The conduction-band velocities in WO₃ are indeed much larger than those in STO, for each of the t_{2g} bands. This combination of factors leads to a larger scattering rate and lower mobility in STO.

IV. CONCLUSIONS

In conclusion, we have used first-principles calculations to investigate the transport properties in WO₃. We consider the full $\bf k$ dependence of the scattering rates to compute the conductivity tensor based on Boltzmann transport theory. Mobilities were calculated as a function of doping level for carrier concentrations ranging from 10^{18} to 10^{21} cm⁻³. We find mobilities as high as 485 cm² V⁻¹ s⁻¹ at 10^{20} cm⁻³ doping. Finally, we show that the enhanced mobilities in WO₃ relative to the widely studied STO can be attributed to one fewer polar LO mode, larger phonon frequencies, and larger band velocities for WO₃.

ACKNOWLEDGMENTS

We thank B. Himmetoglu for early contributions, fruitful discussions, and guidance. This work was supported by the Office of Naval Research (ONR) under Grants No. N00014-12-1-0976 (EXEDE MURI) and No. N00014-18-1-2704. W.W. acknowledges a Graduate Research Fellowship from the National Science Foundation (NSF) under Grant No. DGE 1144085. Use was made of computational facilities purchased with funds from NSF (CNS-1725797) and administered by the Center for Scientific Computing, which is supported by the California NanoSystems Institute and the Materials Research Science and Engineering Center (MRSEC; NSF DMR 1720256) at UC Santa Barbara. We also acknowledge computaional resources provided by the Extreme Science and Engineering Discovery Environment (XSEDE), which is supported by NSF under Grant No. ACI-1548562, and by the DOD High Performance Computing Modernization Program at the AFRL DSRC and ERDC DSRC under Project No. ONRDC36953418.

^[1] P. Zubko, S. Gariglio, M. Gabay, P. Ghosez, and J.-M. Triscone, Annu. Rev. Condens. Matter Phys. **2**, 141 (2011).

^[2] J. A. Sulpizio, S. Ilani, P. Irvin, and J. Levy, Annu. Rev. Mater. Res. 44, 117 (2014).

^[3] S. K. Deb, Appl. Opt. 8, 192 (1969).

^[4] C.G. Granqvist, J. Eur. Ceram. Soc. 25, 2907 (2005).

^[5] R.-T. Wen, C. G. Granqvist, and G. A. Niklasson, Nat. Mater. 14, 996 (2015).

^[6] Q. Zhong, J. R. Dahn, and K. Colbow, Phys. Rev. B 46, 2554 (1992).

^[7] B. W. Brown and E. Banks, J. Am. Chem. Soc. 76, 963 (1954).

^[8] A. Staerz, U. Weimar, and N. Barsan, Sensors 16, 1815 (2016).

- [9] Y. Ping, Y. Li, F. Gygi, and G. Galli, Chem. Mater. 24, 4252 (2012).
- [10] J. Takashima, N. Oka, and Y. Shigesato, Jpn. J. Appl. Phys. 51, 055501 (2012).
- [11] S. Yoon, C. Jo, S. Y. Noh, C. W. Lee, J. H. Song, and J. Lee, Phys. Chem. Chem. Phys. 13, 11060 (2011).
- [12] K. Mahmood, B. S. Swain, A. R. Kirmani, and A. Amassian, J. Mater. Chem. A 3, 9051 (2015).
- [13] J. M. Berak and M. J. Sienko, J. Solid State Chem. 2, 109 (1970).
- [14] L. Berggren, Ph.D. thesis, Uppsala University, 2004.
- [15] K. R. Locherer, I. P. Swainson, and E. K. H. Salje, J. Phys. Condens. Matter 11, 6737 (1999).
- [16] L. Bjaalie, B. Himmetoglu, L. Weston, A. Janotti, and C. G. Van de Walle, New J. Phys. 16, 025005 (2014).
- [17] K. Krishnaswamy, L. Bjaalie, B. Himmetoglu, A. Janotti, L. Gordon, and C. G. Van de Walle, Appl. Phys. Lett. 108, 083501 (2016).
- [18] Y. Du, M. Gu, T. Varga, C. Wang, M. E. Bowden, and S. A. Chambers, ACS Appl. Mater. Interfaces 6, 14253 (2014).
- [19] A. Garg, J. A. Leake, and Z. H. Barber, J. Phys. D Appl. Phys. 33, 1048 (2000).
- [20] R. Clarke, Phys. Rev. Lett. 39, 1550 (1977).
- [21] A. D. Walkingshaw, N. A. Spaldin, and E. Artacho, Phys. Rev. B 70, 165110 (2004).
- [22] W. Wang, A. Janotti, and C. G. Van de Walle, J. Chem. Phys. 146, 214504 (2017).
- [23] J. Ziman, Electrons and Phonons: The Theory of Transport Phenomena in Solids (Oxford University Press, London, 1967).
- [24] F. Giustino, M. L. Cohen, and S. G. Louie, Phys. Rev. B 76, 165108 (2007).
- [25] F. Giustino, Rev. Mod. Phys. 89, 015003 (2017).
- [26] S. Poncé, E. Margine, C. Verdi, and F. Giustino, Comput. Phys. Commun. 209, 116 (2016).
- [27] C. Verdi and F. Giustino, Phys. Rev. Lett. 115, 176401 (2015).
- [28] J. Son, P. Moetakef, B. Jalan, O. Bierwagen, N. J. Wright, R. Engel-Herbert, and S. Stemmer, Nat. Mater. 9, 482 (2010).
- [29] B. Himmetoglu, A. Janotti, H. Peelaers, A. Alkauskas, and C. G. Van de Walle, Phys. Rev. B **90**, 241204(R) (2014).
- [30] P. Giannozzi, S. Baroni, N. Bonini, M. Calandra, R. Car, C. Cavazzoni, D. Ceresoli, G. L. Chiarotti, M. Cococcioni, I. Dabo, A. Dal Corso, S. de Gironcoli, S. Fabris, G. Fratesi, R. Gebauer, U. Gerstmann, C. Gougoussis, A. Kokalj, M. Lazzeri, L. Martin-Samos, N. Marzari, F. Mauri, R. Mazzarello, S. Paolini, A. Pasquarello, L. Paulatto, C. Sbraccia, S. Scandolo, G. Sclauzero, A. P. Seitsonen, A. Smogunov, P. Umari, and R. M. Wentzcovitch, J. Phys. Condens. Matter 21, 395502 (2009).
- [31] N. Troullier and J. L. Martins, Phys. Rev. B 43, 1993 (1991).
- [32] J. P. Perdew, K. Burke, and M. Ernzerhof, Phys. Rev. Lett. 77, 3865 (1996).
- [33] J. Heyd, G. E. Scuseria, and M. Ernzerhof, J. Chem. Phys. 118, 8207 (2003).
- [34] J. Heyd, G. E. Scuseria, and M. Ernzerhof, J. Chem. Phys. 124, 219906 (2006).

- [35] S. Baroni, S. de Gironcoli, A. Dal Corso, and P. Giannozzi, Rev. Mod. Phys. 73, 515 (2001).
- [36] J.J. Zhou, O. Hellman, and M. Bernardi, Phys. Rev. Lett. 121, 226603 (2018).
- [37] A. Dal Corso and A. Mosca Conte, Phys. Rev. B 71, 115106 (2005).
- [38] G. K. Madsen and D. J. Singh, Comput. Phys. Commun. 175, 67 (2006).
- [39] B. Himmetoglu and A. Janotti, J. Phys. Condens. Matter 28, 065502 (2016).
- [40] J. J. Zhou and M. Bernardi, Phys. Rev. B 94, 201201(R) (2016).
- [41] J. Zhou, B. Liao, and G. Chen, Semicond. Sci. Technol. 31, 043001 (2016).
- [42] K. Krishnaswamy, B. Himmetoglu, Y. Kang, A. Janotti, and C. G. Van de Walle, Phys. Rev. B **95**, 205202 (2017).
- [43] Y. Kang, K. Krishnaswamy, H. Peelaers, and C. G. Van de Walle, J. Phys. Condens. Matter 29, 234001 (2017).
- [44] H. Fröhlich, Adv. Phys. 3, 325 (1954).
- [45] P. Vogl, Phys. Rev. B 13, 694 (1976).
- [46] J. Sjakste, N. Vast, M. Calandra, and F. Mauri, Phys. Rev. B 92, 054307 (2015).
- [47] H. Peelaers, E. Kioupakis, and C. G. Van de Walle, Phys. Rev. B 92, 235201 (2015).
- [48] E. Kioupakis, P. Rinke, A. Schleife, F. Bechstedt, and C. G. Van de Walle, Phys. Rev. B 81, 241201(R) (2010).
- [49] B. K. Ridley, Quantum Processes in Semiconductors, 3rd ed. (Oxford University Press, New York, 1993), p. 378.
- [50] W. A. Crichton, P. Bouvier, and A. Grzechnik, Mater. Res. Bull. 38, 289 (2003).
- [51] R. Chatten, A. V. Chadwick, A. Rougier, and P. J. D. Lindan, J. Phys. Chem. B 109, 3146 (2005).
- [52] J. Paier, M. Marsman, K. Hummer, G. Kresse, I. C. Gerber, and J. G. Ángyán, J. Chem. Phys. 124, 154709 (2006).
- [53] W. Wang, A. Janotti, and C. G. Van de Walle, J. Mater. Chem. C 4, 6641 (2016).
- [54] M. S. Dresselhaus, G. Dresselhaus, and A. Jorio, Group Theory: Applications to the Physics of Condensed Matter (Springer, New York, Berlin, 2008), p. 582.
- [55] H. Hamdi, E. K. H. Salje, P. Ghosez, and E. Bousquet, Phys. Rev. B 94, 245124 (2016).
- [56] J. L. Servoin, Y. Luspin, and F. Gervais, Phys. Rev. B 22, 5501 (1980).
- [57] W. G. Stirling and R. Currat, J. Phys. C Solid State Phys. 9, L519 (1976).
- [58] S. K. Deb, Philos. Mag. 27, 801 (1973).
- [59] W. G. Spitzer, R. C. Miller, D. A. Kleinman, and L. E. Howarth, Phys. Rev. 126, 1710 (1962).
- [60] M. Bernardi, D. Vigil-Fowler, C. S. Ong, J. B. Neaton, and S. G. Louie, Proc. Natl. Acad. Sci. USA 112, 5291 (2015).
- [61] A. Janotti, D. Steiauf, and C. G. Van de Walle, Phys. Rev. B 84, 201304(R) (2011).
- [62] M. Marques, L. K. Teles, V. Anjos, L. M. R. Scolfaro, J. R. Leite, V. N. Freire, G. A. Farias, and E. F. da Silva, Appl. Phys. Lett. 82, 3074 (2003).